Journal of Computational Physics **173,** 512–526 (2001)
doi:10.1006/jcph.2001.6890, available online at http://www.idealibrary.com on IDEAL®

The Treatment of Reacting Surfaces for Finite-Volume Schemes on Unstructured Meshes

Sandip Mazumder and Samuel A. Lowry

CFD Research Corporation, Huntsville, Alabama 35805
E-mail: sm@cfdrc.com

Received September 12, 2000; revised July 19, 2001

A rigorous and robust numerical procedure to treat surface reaction boundary conditions for finite-volume schemes in unstructured meshes is presented. The procedure is applicable to arbitrary cell topologies and multistep finite-rate surface reactions of arbitrary complexity. The accuracy of the numerical procedure has been verified by systematically comparing solutions obtained using unstructured meshes with perfectly orthogonal meshes for both two-dimensional and three-dimensional geometries. Validation results presented for gallium arsenide growth in a full-scale commercial metal organic-chemical vapor-deposition reactor, exhibit excellent match with experimental data. © 2001 Academic Press

Key Words: finite-volume; unstructured mesh; surface reaction; chemical vapor deposition.

NOMENCLATURE

a_{ij}, b_{ij}	stoichiometric coefficients
A_S	surface area (m^2)
D_k	mass diffusion coefficient of kth species (m^2/s)
J_S	Stefan flux (kg/m^2/s)
$\mathbf{J}_k$	diffusion flux of kth species (kg/m^2/s)
k_f, k_r	forward and reverse rate constants, respectively
$\hat{\mathbf{l}}$	unit vector connecting face center to cell center
M_k	molecular weight of kth species (kg/kmol)
$\hat{\mathbf{n}}$	unit surface normal
N_g	number of gas-phase species
N_S	number of surface-adsorbed species
N_b	number of bulk species
N_{steps}	number of steps in surface reaction mechanism

0021-9991/01 $35.00
Copyright © 2001 by Academic Press
All rights of reproduction in any form reserved.

$\dot{S}_k$ production rate of kth species (kmol/m^2/s)
t time (s)
$\Im$ tangential component of diffusion flux (kg/m^2/s)
$\mathbf{U}_S$ Stefan velocity (m/s)
V volume of cell (m^3)
$\mathbf{V}_k$ diffusion velocity (m/s)
X_k site fraction of kth species
Y_k mass fraction of kth species

Greek

δ diffusion length-scale (m)
Λ_k molar concentration of kth species (kmol/m^2)
ρ mass density (kg/m^3)
ρ_S surface site density (kmol/m^2)

Subscripts

C cell center
W wall (or reacting surface)
f face

Superscripts

$'$ reactants
$''$ products

1. INTRODUCTION

Many important technologies involve chemical reactions at solid surfaces. These include wafer processing by chemical vapor deposition (CVD) or etching [1–18], DNA separation [19], and catalytic combustion [20, 21], among many others. During the past two decades or so, numerical modeling has gained tremendous popularity in the semiconductor material processing area [5–12]. This can be attributed in part to modern, high-speed, affordable computers and in part to the increased understanding of the chemical processes underlying semiconductor growth. In the semiconductor as well as the automotive industry, computational fluid dynamics (CFD) based tools are now used routinely to study thin film growth and catalytic combustion processes.

One of the main reasons CFD tools have not evolved as the most important design tool is the complexity associated with grid generation for real-life reactor chambers. For example, a typical commercial metal organic-chemical vapor-deposition (MOCVD) reactor has helical induction coils around it (Fig. 1). These need to be modeled along with the rest of the reactor to predict the current densities and consequently the joule heating in the substrate. It goes without saying that generation of a grid for such three-dimensional (3D) geometry is more than an uphill task for a nonspecialist. During the past decade or so, it has been realized that the grid generation problem can be alleviated by using unstructured meshes, as opposed to multidomain body-fitted grids. Not only is the grid generation technology for unstructured meshes quite mature (thanks to finite element methods!), but also it allows

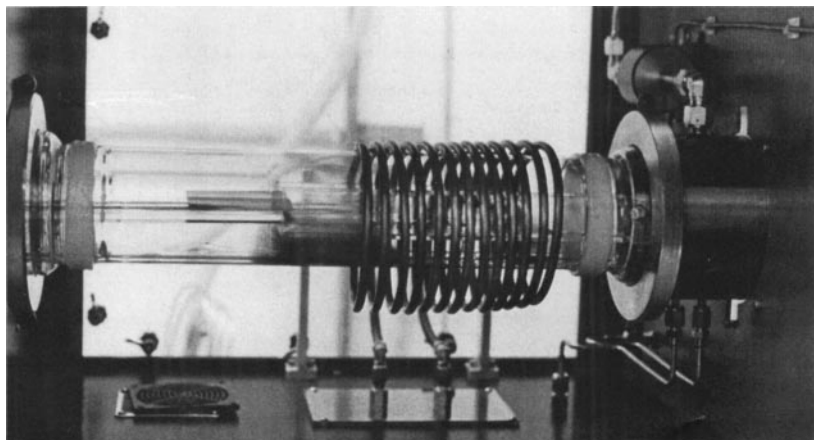

FIG. 1. Photograph of a commercial horizontal MOCVD reactor (Crystal Specialties Model 425) showing copper induction coils around the reactor.

tremendous advantages for complex geometries. With the growing need for modeling full-scale industrial reactors, it is fair to say now that unstructured meshes are the ones of choice, at least in some parts of the computational domain.

The numerical treatment of reacting surfaces in finite-volume schemes is straightforward if the grid next to the surface is orthogonal. This has been discussed and implemented by a number of researchers in the past for simple geometries [5–10]. Complexities arise when the boundary surfaces are irregular in shape and the grids adjacent to them are nonorthogonal. (Since unstructured grids are usually nonorthogonal, henceforth we will refer to nonorthogonal meshes as "unstructured.") This article presents a numerical procedure to treat surface reaction boundary conditions at surfaces that have unstructured meshes adjacent to them. The procedure outlined here is applicable to any arbitrary grid topology in both two and three dimensions. In addition, it provides a detailed description of the numerical schemes required for the treatment of complex surface chemistry, including surface-adsorbed species.

2. MATHEMATICAL FORMULATION

2.1. *Reaction–Diffusion Balance at Surface*

At any stationary solid surface, the bulk flow velocity is zero (no-slip condition), and diffusion is the only mechanism for species transport to and from the surface. In the absence of chemical reactions at the surface, the net diffusive exchange of species between the gas phase and the solid surface is zero, and the cell-center concentration of the species will be identical to the near-wall concentrations. If reactions occur at the surface, the near-wall species concentrations will be determined by the balance of the reaction and diffusion fluxes. Mathematically this may be expressed as [11]

$$\hat{\mathbf{n}} \cdot [\rho(\mathbf{U}_\mathrm{S} + \mathbf{V}_k)Y_k] = M_k \dot{S}_k \qquad \forall k = 1, 2, \ldots, N_\mathrm{g}, \tag{1}$$

where $\hat{\mathbf{n}}$ is the unit surface normal pointing from the boundary into the computational domain (Fig. 2), N_g is the total number of gas-phase species, ρ is the mixture density, and Y_k and M_k are the mass-fraction and molecular weight of the kth species, respectively.

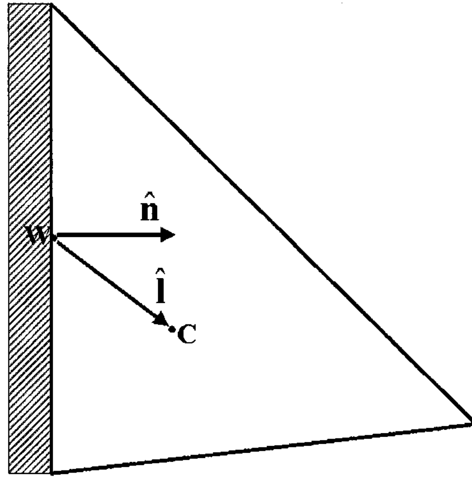

FIG. 2. Schematic of a control-volume next to a wall showing the surface normal and the vector connecting the face center with the cell center. The surface (or wall) is denoted by W and the cell center is denoted by C.

The production rate of the kth species, $\dot{S}_k$, due to chemical reaction at the surface, is a complex, nonlinear function of the species mass-fractions and is discussed in detail later. The diffusion flux of the kth species, $\mathbf{J}_k$, may be written using Fick's law as [11]

$$\mathbf{J}_k = \rho \mathbf{V}_k Y_k = \rho D_k \nabla Y_k, \tag{2}$$

where $\mathbf{V}_k$ is the so-called diffusion velocity. Summation of Eq. (1) over all gas-phase species yields

$$J_{\mathrm{S}} = \rho \hat{\mathbf{n}} \cdot \mathbf{U}_S = \sum_{k=1}^{N_{\mathrm{g}}} M_k \dot{S}_k, \tag{3}$$

since $\sum_{k=1}^{N_{\mathrm{g}}} \mathbf{J}_k = 0$ by definition. $\mathbf{U}_S$ is the so-called Stefan velocity, and $J_{\mathrm{S}} = \rho \hat{\mathbf{n}} \cdot \mathbf{U}_S$ is the so-called Stefan flux, normal to the surface. In the absence of deposition/etching, the Stefan flux is identically equal to zero. Equation (1), after rearrangement and substitution of Eqs. (2) and (3), may be rewritten as

$$\hat{\mathbf{n}} \cdot [\rho D_k \nabla Y_k] = M_k \dot{S}_k - J_{\mathrm{S}} Y_k. \tag{4}$$

Now consider the finite-volume cell shown in Fig. 2. $\hat{\mathbf{n}}$ is the unit surface normal of the boundary face, and $\hat{\mathbf{l}}$ is the vector pointing from the face center of the boundary face, depicted by W, to the cell center of the adjacent cell, depicted by C. The discretization of the term on the left-hand side of Eq. (4) is fairly straightforward if the grid is Cartesian (i.e., if the vectors $\hat{\mathbf{n}}$ and $\hat{\mathbf{l}}$ are aligned), or if a transformation is invoked whereby the entire geometry is transformed to a body-fitted coordinate system. The latter is not possible for an unstructured grid, and the former is a rare occurrence for problems of practical interest. The more common scenario is when $\hat{\mathbf{n}}$ and $\hat{\mathbf{l}}$ are misaligned. The right-hand side of Eq. (2) may also be written as

$$\rho D_k \nabla Y_k = (\rho D_k \nabla Y_k \cdot \hat{\mathbf{n}})\hat{\mathbf{n}} + (\hat{\mathbf{n}} \times \rho D_k \nabla Y_k) \times \hat{\mathbf{n}}. \tag{5}$$

Performing a dot-product of Eq. (5) with the vector $\hat{\mathbf{l}}$ yields

$$(\rho D_k \nabla Y_k) \cdot \hat{\mathbf{l}} = (\rho D_k \nabla Y_k \cdot \hat{\mathbf{n}})\hat{\mathbf{n}} \cdot \hat{\mathbf{l}} + [(\hat{\mathbf{n}} \times \rho D_k \nabla Y_k) \times \hat{\mathbf{n}}] \cdot \hat{\mathbf{l}}. \tag{6}$$

The quantity $\hat{\mathbf{n}} \cdot \hat{\mathbf{l}}$ can be computed easily since both vectors are known directly from the geometry or grid information. It represents the normal distance from the cell center to the boundary and is, henceforth, denoted by δ. Equation (6) now can be written in discretized form as

$$\rho D_k (Y_{k,C} - Y_{k,W}) = (\rho D_k \nabla Y_k \cdot \hat{\mathbf{n}})\delta + \Im, \tag{7}$$

where $Y_{k,C}$ and $Y_{k,W}$ are the cell center and near-wall mass-fractions, respectively, of the kth species. $\Im$ represents the last term of Eq. (6) and physically represents the tangential component of the diffusion flux at the surface. The first term on the right-hand side of Eq. (7) represents the normal component of the diffusion flux to the surface. Using Eqs. (7) and (4), this term can be rewritten as

$$\rho D_k \nabla Y_k \cdot \hat{\mathbf{n}} = \frac{\rho D_k (Y_{k,C} - Y_{k,W})}{\delta} - \frac{\Im}{\delta} = M_k \dot{S}_k - J_S Y_k. \tag{8}$$

The computation of the tangential component of the diffusion flux, $\Im$, is not straightforward and requires further examination. It can be computed by invoking the assumption that the tangential component of the diffusion flux at the wall is same as that at the cell center adjacent to the wall. This is nearly true for most applications, where the gradients are strong in the direction normal to the wall (due to surface reaction) but are weak along the wall. In any case, the assumption introduces a second-order error in computation. By this approximation, $\Im$ may be written as

$$\Im = [(\hat{\mathbf{n}} \times \rho D_k \nabla Y_k|_W) \times \hat{\mathbf{n}}] \cdot \hat{\mathbf{l}} \cong [(\hat{\mathbf{n}} \times \rho D_k \nabla Y_k|_C) \times \hat{\mathbf{n}}] \cdot \hat{\mathbf{l}}. \tag{9}$$

The gradient at the cell center can be computed using the Gauss divergence theorem, and Eq. (9) may be rewritten as

$$\Im = \left[\hat{\mathbf{n}} \times \rho D_k \left(\frac{1}{V} \sum_f A_f Y_{k,f} \hat{\mathbf{n}}_f\right) \times \hat{\mathbf{n}}\right] \cdot \hat{\mathbf{l}}, \tag{10}$$

where A_f is the face area of face f, $\hat{\mathbf{n}}_f$ is the unit face surface normal, and V is the volume of the cell. The face values of the mass-fraction have been denoted by $Y_{k,f}$ and can be computed by distance-weighted interpolation of the cell-center values for all faces except the boundary face in question, for which it is an unknown. It will be seen shortly that the contribution from that face actually vanishes. Equation (10) can be reduced further and rewritten as

$$\Im = \frac{\rho D_k}{V} \sum_f A_f Y_{k,f} [\hat{\mathbf{n}} \times \hat{\mathbf{n}}_f \times \hat{\mathbf{n}}] \cdot \hat{\mathbf{l}} = \frac{\rho D_k}{V} \sum_f A_f Y_{k,f} [\hat{\mathbf{n}}_f - \hat{\mathbf{n}}(\hat{\mathbf{n}}_f \cdot \hat{\mathbf{n}})] \cdot \hat{\mathbf{l}}. \tag{11}$$

Two important observations must be made at this point. First, for the boundary face in question, $\hat{\mathbf{n}} = \hat{\mathbf{n}}_f$, and the contribution of this face to the summation in Eq. (11) vanishes. Second, for a perfectly Cartesian grid the term vanishes.

2.2. *Surface Reaction Kinetics*

As stated earlier, the molar production rate of the kth species, $\dot{S}_k$, because of chemical reaction at the surface, is a complex nonlinear function of the species mass-fractions. Consider a surface multistep (with N_{steps} steps) surface reaction of the general form

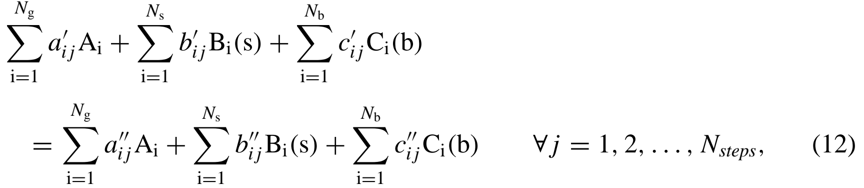

$$\sum_{\mathrm{i}=1}^{N_\mathrm{g}} a'_{ij}\mathrm{A_i} + \sum_{\mathrm{i}=1}^{N_\mathrm{s}} b'_{ij}\mathrm{B_i(s)} + \sum_{\mathrm{i}=1}^{N_\mathrm{b}} c'_{ij}\mathrm{C_i(b)} = \sum_{\mathrm{i}=1}^{N_\mathrm{g}} a''_{ij}\mathrm{A_i} + \sum_{\mathrm{i}=1}^{N_\mathrm{s}} b''_{ij}\mathrm{B_i(s)} + \sum_{\mathrm{i}=1}^{N_\mathrm{b}} c''_{ij}\mathrm{C_i(b)} \qquad \forall j = 1, 2, \ldots, N_{steps}, \tag{12}$$

where a_{ij}, b_{ij} and c_{ij} are stoichiometric coefficients of gas, adsorbed (denoted by (s)), and bulk species (denoted by (b)), respectively. N_g, N_s, and N_b are total numbers of gas-phase, adsorbed, and bulk (deposited or etched) species, respectively. For this reaction, the surface reaction rate may be expressed as [11]

$$\dot{S}_k = \sum_{j=1}^{N_{steps}} \sigma_{kj} \left[k_{fj} \prod_{\mathrm{i}=1}^{N_\mathrm{g}} [\mathrm{A_i}]_\mathrm{w}^{a'_{ij}} \prod_{\mathrm{i}=1}^{N_\mathrm{s}} [\mathrm{B_i(s)}]^{b'_{ij}} - k_{rj} \prod_{\mathrm{i}=1}^{N_\mathrm{g}} [\mathrm{A_i}]_\mathrm{w}^{a''_{ij}} \prod_{\mathrm{i}=1}^{N_\mathrm{s}} [\mathrm{B_i(s)}]^{b''_{ij}} \right], \tag{13}$$

where k_{fj} are forward rates and k_{rj} are reverse rates of the jth step, and the near-wall gas-phase concentrations at the surface are expressed as

$$\Lambda_i = [\mathrm{A_i}]_\mathrm{w} = \frac{\rho_w Y_{i,w}}{M_i} \qquad \forall i = 1, 2, \ldots, N_\mathrm{g} \tag{14}$$

and the surface concentrations are expressed as

$$\Lambda_i = [\mathrm{B_i(s)}] = \rho_s X_i \qquad \forall i = N_\mathrm{g} + 1, \ldots, N_\mathrm{g} + N_\mathrm{s}, \tag{15}$$

with ρ_w and ρ_s being gas-phase mass density and surface site density, respectively. By surface site density, we mean the total surface concentration (in moles per unit area) of all the surface-adsorbed species of a particular type [11]. Y_i and X_i are the gas-phase mass-fractions and surface site fractions, respectively. Λ_i are the molar surface concentrations expressed in moles/area. σ_{kj} is the stoichiometric difference and may be written as

$$\sigma_{kj} = \left\{ \begin{array}{ll} a''_{kj} - a'_{kj} & \forall k = 1, \ldots, N_\mathrm{g} \\ b''_{kj} - b'_{kj} & \forall k = N_\mathrm{g} + 1, \ldots, N_\mathrm{g} + N_\mathrm{s} \end{array} \right\}. \tag{16}$$

Substitution of Eqs. (11) and (13) through (16) into Eq. (8) yields a set of N_g nonlinear simultaneous equations for the near-wall mass-fractions (or molar concentrations) of the gas-phase species. It is generally convenient to use the balance equation on a molar basis, rather than on a mass basis, if one intends to implement chemistry involving surface-adsorbed species. This is because for surface sites, mass is meaningless. Thus, in general, the reaction–diffusion balance equation for the gas-phase species may be rewritten as

$$\frac{D_k[\Lambda_{k,C} - (\rho/\rho_W)\Lambda_{k,W}]}{\delta} - \frac{\Im}{\delta M_k} = \dot{S}_k(\Lambda_{k,W}) - \frac{J_\mathrm{S}\Lambda_{k,W}}{\rho_W} \qquad \forall k = 1, 2, \ldots, N_\mathrm{g}. \tag{17}$$

For surface-adsorbed species, the diffusion flux and Stefan fluxes are zero, and therefore

$$0 = \dot{S}_k(\Lambda_{k,W}) \qquad \forall k = N_\mathrm{g} + 1, \ldots, N_\mathrm{g} + N_\mathrm{s}. \tag{18}$$

The solution of Eqs. (17) and (18) provide the surface (or wall) molar concentrations, $\Lambda_{k,w}$. Once these have been obtained, the diffusion flux (Eq. (2)) can be computed easily. This appears as a source for the control-volume adjacent to the wall in a standard finite-volume scheme. The key issue, thus, is the numerical solution of the set of equations represented by Eqs. (17) and (18).

Equations (17) and (18) may be rewritten in more compact form as

$$\mathbf{f}(\Lambda_i) = 0 \qquad \forall i = 1, 2, \ldots, \mathrm{N_g} + \mathrm{N_s}. \tag{19}$$

Because of the nonlinearity (often strong) of **f**, Eq. (19) cannot be solved by direct inversion and can only be solved by an iterative procedure, such as Newton iteration. Although this follows standard, well-known algorithms and procedures, it is discussed here briefly because certain numerical problems to be discussed shortly require direct reference to the solution technique for Eq. (18). Linearization of Eq. (19), followed by rearrangement, yields

$$\frac{\partial \mathbf{f}}{\partial \mathbf{\Lambda}} \Delta \mathbf{\Lambda} = -\mathbf{f}(\mathbf{\Lambda}_0), \tag{20}$$

where $\mathbf{\Lambda} = \{\Lambda_1, \Lambda_2, \ldots, \Lambda_{N_\mathrm{g}}, \ldots, \Lambda_{N_\mathrm{g}+N_\mathrm{s}}\}$ is the concentration array and the subscript 0 denotes its value at the previous iteration or guess. $\Delta\mathbf{\Lambda}$ is the change in the mass-fraction array, and $\partial\mathbf{f}/\partial\mathbf{\Lambda}$ is the Jacobian matrix. Since Eq. (20) is a linearized form of Eq. (19), it will require successive iterations until the error goes to zero (the Newton iteration procedure). Note that the subscript "w" has been dropped for convenience.

If the surface reaction mechanism is such that only gas-phase species are present, Eq. (19) can be solved "as is" without much difficulty. If, however, the surface chemistry mechanism involves surface-adsorbed species, as is often the case, the system of equations defined by Eq. (19) may be ill-posed, and special treatment is necessary. In order to understand why this occurs, it is easiest to consider an example of a simple surface chemistry mechanism involving surface-adsorbed species. Consider the following two-step mechanism, which often is employed for the CVD of silicon from silane:

Step 1: SiH_4 + OPEN(s) => Si(s) + $2H_2$

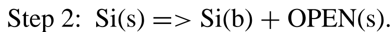
Step 2: Si(s) => Si(b) + OPEN(s).

In the first step, silane gets adsorbed onto an open site to form surface-adsorbed silicon (denoted by (s)) and releases gaseous hydrogen. In the second step, the adsorbed silicon is incorporated into the film as bulk (denoted by (b)) and releases an open site. Let the species be numbered as follows for the sake of convenience: H_2 = 1, SiH_4 = 2, OPEN(s) = 3, SI(s) = 4, and Si(b) = 5. Using Eq. (13), the molar production rate of OPEN(s) and Si(s) may be written as

$$\dot{S}_3 = -k_1\Lambda_2\Lambda_3 + k_2\Lambda_4, \quad \dot{S}_4 = k_1\Lambda_2\Lambda_3 - k_2\Lambda_4, \tag{21}$$

where k_1 and k_2 are forward rate constants of steps 1 and 2, respectively. When substituted into Eq. (18), we get two equations, which are identical, and thus the system of equations, described by Eq. (19) is ill-posed. The problem may be circumvented by introducing a pseudotransient solution procedure. Equation (18) is valid only at steady state. For transient calculations, one has to account for the "storage" of surface-adsorbed species. The residence time of a species at the surface will depend on the relative time-scales of adsorption and desorption. For such a case, Eq. (18) may be appropriately modified to

$$\frac{\partial \Lambda_{k,W}}{\partial t} = A_S \dot{S}_k(\Lambda_{k,W}) \qquad \forall k = N_{\mathrm{g}} + 1, \ldots, N_{\mathrm{g}} + N_{\mathrm{s}}, \tag{22}$$

where A_S is the surface area. The transient term vanishes at steady state. In the current numerical scheme, instead of eliminating that term for steady state calculations, we rewrite it in discretized form as

$$\frac{\Lambda_{k,W} - \Lambda^*_{k,W}}{\Delta t} = A_S \dot{S}_k(\Lambda_{k,W}) \qquad \forall k = N_{\mathrm{g}} + 1, \ldots, N_{\mathrm{g}} + N_{\mathrm{s}}, \tag{23}$$

where $\Lambda^*_{k,W}$ is the value of the wall concentration at the previous time step for transient calculations and the value of the wall concentration at the previous iteration for steady state calculations. When linearization is once again implemented, instead of Eq. (20) we have an equation of the following form for the surface-adsorbed species. (i.e., $N_{\mathrm{g}} + 1 \leq i \leq N_{\mathrm{g}} + N_{\mathrm{s}}$):

$$\left(\frac{1}{\Delta t} + \frac{\partial \mathbf{f}}{\partial \boldsymbol{\Lambda}}\right) \Delta \boldsymbol{\Lambda} = -\left(\mathbf{f}(\boldsymbol{\Lambda}_0) + \frac{\boldsymbol{\Lambda} - \boldsymbol{\Lambda}^*}{\Delta t}\right). \tag{24}$$

At steady state $\Delta\Lambda = 0$, and Eq. (19) is recovered. For steady state calculations, any arbitrary value can be assigned to Δt. The additional pseudotransient term actually serves to relax the equations, and thus the value of Δt represents how strong the relaxation is. The smaller the value of Δt, the larger is the relaxation applied to the equation. In practice, it was found that a value of $\Delta t = 1$ keeps the equation system stable for even very complex mechanisms. This numerical treatment of introducing a pseudotransient term for the surface-adsorbed species for steady state computations removes the "ill-posed-ness" of the equations described earlier.

All of these models and schemes were implemented into the commercial unstructured finite-volume CFD code, CFD-ACE+. The governing equations are the equations of conservation of mass, momentum, energy, and species. Detailed discussion of the governing equations may be found elsewhere [8, 9, 22].

3. RESULTS AND DISCUSSION

The accuracy and effectiveness of the numerical scheme described earlier for unstructured meshes was first verified by systematically comparing results obtained from unstructured grid computations with those obtained using perfectly orthogonal (nonskewed) grids. Following these studies, validation studies were conducted for a full-scale industrial MOCVD

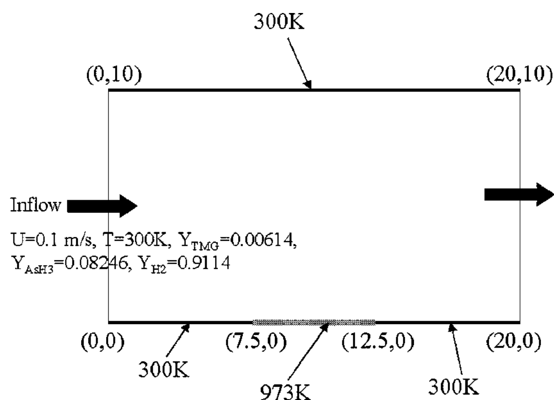

FIG. 3. Geometry and boundary conditions for two-dimensional verification study. Coordinates shown are in centimeters.

reactor to highlight the accuracy of the overall surface reaction boundary treatment discussed in Section 2.

The verification studies were first performed for a relatively simple two-dimensional geometry, which is shown in Fig. 3. The boundary conditions also are depicted on the same figure. Computations were performed in this geometry using perfectly orthogonal quadrilateral elements as well as unstructured triangular elements to study gallium arsenide deposition. The reaction mechanisms used for the simulations consisted of an 11-step gas-phase reaction mechanism (Table I) and a 25-step surface chemistry mechanism (Table II).

TABLE I
Gas Phase Reactions for Multistep GaAs Mechanism

No.	Gas-phase reaction	A	E/R	n	Source for reaction rate
G1	$TMG \leftrightarrow CH_3 + DMG$	1.6E17	30057	0	Tirtowidjojo and Pollard [14, 15]
G2	$DMG \leftrightarrow CH_3 + MMG$	2.5E15	17883	0	Tirtowidjojo and Pollard [14, 15]
G3	$CH_3 + H_2 \leftrightarrow CH_4 + H$	1.2E9	6300	0	Tirtowidjojo and Pollard [14, 15]
G4	$AsH_3 + CH_3 \leftrightarrow AsH_2 + CH_4$	9.7E8	900	0	Jensen *et al.* [3], Ern *et al.* [9]
G5	$TMG + H \leftrightarrow DMG + CH_4$	5.0E10	5051	0	Jensen *et al.* [3], Ern *et al.* [9]
G6	$DMG + H \leftrightarrow MMG + CH_4$	5.0E10	5051	0	Jensen *et al.* [3]; Ern *et al.* [9]
G7	$2H + M \leftrightarrow H_2 + M$	1.0E13	0	0	Jensen *et al.* [3]; Ern *et al.* [9]
G8	$2CH_3 \leftrightarrow C_2H_6$	2.0E10	0	0	Jensen *et al.* [3]; Ern *et al.*[9]
G9	$CH_3 + H + M \leftrightarrow CH_4 + M$	2.4E19	0	−1	Jensen *et al.* [3]; Ern *et al.* [9]
G10	$TMG + CH_3 \leftrightarrow ADDUCT + CH_4$	2.0E8	5051	0	Jensen *et al.* [3]; Ern *et al.* [9]
G11	$MMG \leftrightarrow Ga + CH_3$	1.0E16	39052	0	Tirtowidjojo and Pollard [14, 15]

Note: Reactions G1 and G2 have been known to be pressure dependent (Tirtowidjojo and Pollard [14, 15]). The values of A, provided here, are at 1 atm. The reactions that lead to GaC formation have been eliminated from Jensen's mechanism to simplify the chemistry. The net effect of all these subsidiary reactions has been modeled using G10, which is necessary to consume some quantity of TMG. The product ADDUCT can be a single complex or a combination of complex intermediate products. G11 was included to model the formation of gallium (maybe liquid) and its subsequent direct adsorption (see surface chemistry reactions S24 and S25). The reverse rates were calculated by minimization of the Gibb's free energy. The rate constant A has units of 1/s for unimolecular reactions and m^3.s/kmol for bimolecular reactions. DMG and MMG are dimethyl and monomethyl gallium, respectively. M refers to a third body.

TABLE II
Surface Reactions for Deposition of GaAs from Trimethyl Gallium (TMG) and Arsine

No.	Surface reaction	A	E/R	n	Source for reaction rate
S1	$H + SG \rightarrow HG(s)$	4.95E9	0	0.5	Jensen *et al.* [3], Ern *et al.* [9]
S2	$H + SA \rightarrow HA(s)$	4.95E9	0	0.5	Jensen *et al.* [3], Ern *et al.* [9]
S3	$CH_3 + SA \rightarrow CH_3A(s)$	1.27E9	0	0.5	Jensen *et al.* [3], Ern *et al.* [9]
	$CH_3 + SA \leftarrow CH_3A(s)$	1.0E12	10103	0	Tirtowidjojo and Pollard [14, 15]
S4	$CH_3 + SG \rightarrow CH_3G(s)$	1.27E9	0	0.5	Jensen *et al.* [3], Ern *et al.* [9]
	$CH_3 + SG \leftarrow CH_3G(s)$	1.0E12	10103	0	Tirtowidjojo and Pollard [14, 15]
S5	$MMG + SG \rightarrow MMG(s)$	5.37E8	0	0.5	Jensen *et al.* [3], Ern *et al.* [9]
	$MMG + SG \leftarrow MMG(s)$	1.0E13	20206	0	Tirtowidjojo and Pollard [14, 15]
S6	$DMG + SG \rightarrow MMG(s) + CH_3$	4.95E8	0	0.5	Jensen *et al.* [3], Ern *et al.* [9]
S7	$AsH + SA \rightarrow AsH(s)$	5.68E8	0	0.5	Jensen *et al.* [3], Ern *et al.* [9]
	$Ash + SA \leftarrow AsH(s)$	1.0E13	20206	0	Tirtowidjojo and Pollard [14, 15]
S8	$AsH_2 + SA \rightarrow AsH(s) + H$	5.68E8	0	0.5	Jensen *et al.* [3], Ern *et al.* [9]
S9	$AsH_3 + SA \rightarrow AsH(s) + H_2$	5.68E8	0	0.5	Jensen *et al.* [3], Ern *et al.* [9]
S10	$CH_3 + HG(s) \rightarrow CH_4 + SG$	1.26E8	0	0.5	Jensen *et al.* [3], Ern *et al.* [9]
S11	$CH_3 + HA(s) \rightarrow CH_4 + SA$	1.26E8	0	0.5	Jensen *et al.* [3], Ern *et al.* [9]
S12	$H + CH_3G(s) \rightarrow CH_4 + SG$	4.94E8	0	0.5	Jensen *et al.* [3], Ern *et al.* [9]
S13	$H + CH_3A(s) \rightarrow CH_4 + SA$	4.94E8	0	0.5	Jensen *et al.* [3], Ern *et al.* [9]
S14	$HG(s) + CH_3A(s) \rightarrow CH_4 + SA + SG$	1.0E16	5051	0	Jensen *et al.* [3], Ern *et al.* [9]
S15	$HA(s) + CH_3G(s) \rightarrow CH_4 + SA + SG$	1.0E16	5051	0	Jensen *et al.* [3], Ern *et al.* [9]
S16	$HA(s) + HG(s) \rightarrow H_2 + SA + SG$	1.2E16	10102	0	Jensen *et al.* [3], Ern *et al.* [9]
S17	$CH_2A(s) + CH_3G(s) \rightarrow C_2H_6 + SA + SG$	1.0E16	10102	0	Jensen *et al.* [3], Ern *et al.* [9]
S18	$MMG(s) + AsH(s) \rightarrow CH_4 + SA + SG + GaAs(b)$	5.0E17	14801	0	Jensen *et al.* [3], Ern *et al.* [9]
S19	$MMG(s) + As(s) \rightarrow CH_3 + SA + SG + GaAs(b)$	5.0E17	10103	0	Jensen *et al.* [3], Ern *et al.* [9]
S20	$2AsH(s) \rightarrow As_2 + H_2 + 2SA$	1.0E16	19681	0	Jensen *et al.* [3], Ern *et al.* [9]
S21	$CH_3 + AsH(s) \rightarrow As(s) + CH_4$	1.28E8	10103	0.5	Jensen *et al.* [3], Ern *et al.* [9]
S22	$2As(s) \rightarrow As_2 + 2SA$	1.0E17	15155	0	Jensen *et al.* [3], Ern *et al.* [9]
	$2As(s) \leftarrow As_2 + 2SA$	1.0E29	15155	0	calibrated
S23	$TMG + SG \rightarrow MMG(s) + 2CH_3$	4.62E8	0	0.5	Jensen *et al.* [3], Ern *et al.* [9]
S24	$Ga + SG \rightarrow Ga(s)$	5.9E8	0	0.5	Ingle *et al.* [10]
	$Ga + SG \leftarrow Ga(s)$	1.0E13	22732	0	Ingle *et al.* [10]
S25	$Ga(s) + As(s) \rightarrow SA + SG + GaAs(b)$	1.1E9	505	0	Ingle *et al.* [10]

Note: The reactions with $E/R = 0$ have rates based on a sticking coefficient, which has been converted to a general rate with a temperature exponent of 0.5. S24 and S25 have been added to Jensen's mechanism to model adsorption–desorption kinetics of gallium at high temperatures. The rate constants are in SI units (kmol, K, J, m, s.). SA and SG are open arsenic and gallium sites, respectively. Both types of sites have a total site concentration of 7.34×10^{-9} kmol/m^2. (s) denotes an adsorbed species. (b) denotes a deposited bulk species. $CH_3G(s)$ and $CH_3A(s)$ represent adsorbed CH_3 radicals on gallium and arsenic sites, respectively. The same nonmenclature has been used for adsorbed hydrogen radicals.

Such complex chemistry was chosen to emphasize the ability of the above numerical scheme to treat extremely stiff and complex reaction kinetics, which is a common occurrence for commercial applications. The details pertaining to the reaction mechanism used here may be found elsewhere [22]. The grid was refined in several stages to obtain grid-independent solutions. Figure 4 shows simulation results obtained using quadrilateral (structured) and triangular (unstructured) grid elements for the two final stages of refinement. It is clear

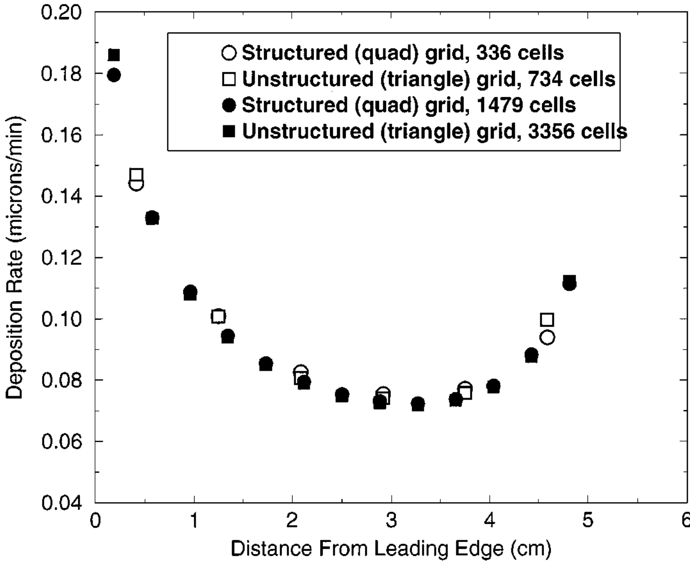

FIG. 4. Deposition rate of gallium arsenide on substrate for two-dimensional geometry.

from this figure that the results are practically independent of what type of grid was used for the simulations. Similar studies also were performed for a simple 3D geometry (Fig. 5) using tetrahedral (unstructured) finite-volume cells and perfectly orthogonal hexahedral cells. These results were obtained using a simple one-step surface reaction mechanism [4] to minimize computational time requirements. The results are depicted in Fig. 6. Once again, it is seen that the results obtained by orthogonal and skewed grids are in close agreement.

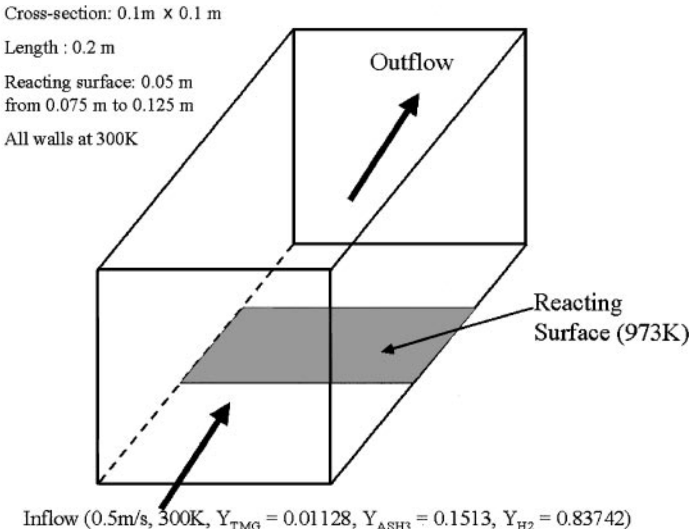

FIG. 5. Geometry and boundary conditions used for three-dimensional verification study.

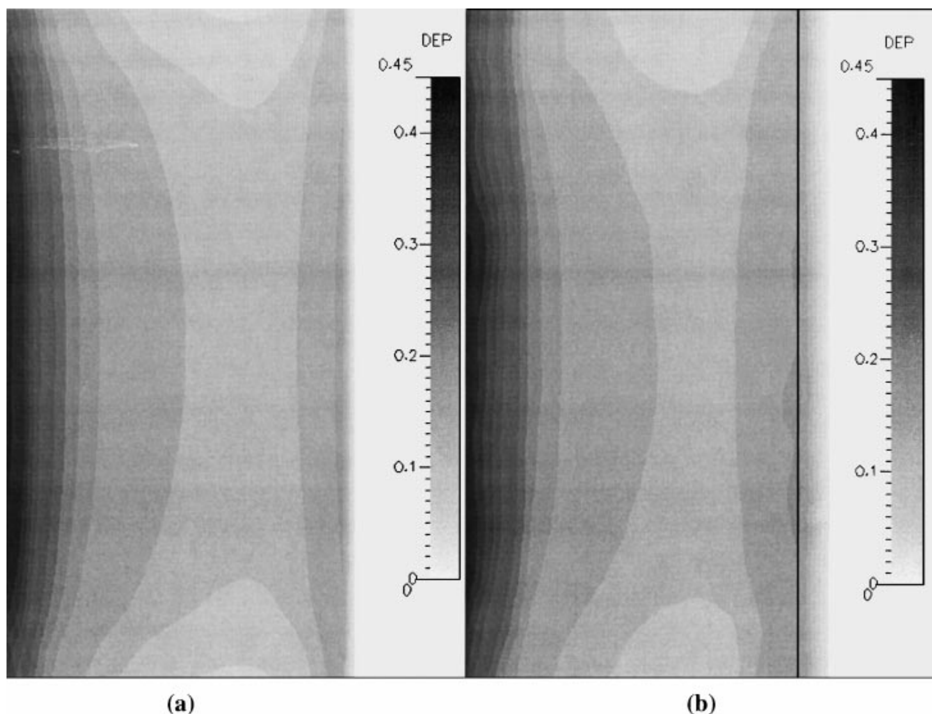

FIG. 6. Deposition rate of gallium arsenide on substrate for three-dimensional geometry: (a) structured grid (37,600 hexahedral cells), (b) unstructured grid (42,270 tetrahedral cells).

Following these studies, computations were performed on a full-scale commercial MOCVD reactor. The actual reactor geometry, its 2D computer model, and the unstructured triangular grid are shown in Fig. 7. Simulations were performed in this reactor using boundary conditions that mimic the actual operating conditions, which were used to collect experimental data [4]. In addition to solution of the equations of conservation of mass, momentum energy, and species, the equation of radiative transport was solved using a Monte Carlo approach, which was developed as part of a separate study [23, 24]. Since the substrate is at 973 K and is surrounded by a cold medium (300 K), the dominant mode of heat loss from it is by radiation. The radiative energy impinges on the reactor walls made of fused silica, causing the temperature of these walls to go up to about 600 K. This results in parasitic deposition on the reactor walls, a surface phenomenon, which is rate-limited and is described elsewhere [6, 13, 22]. It is important to note that rate-limited parasitic deposition on reactor walls has to be predicted accurately in order to correctly predict deposition on the target substrate [22]. The species mass diffusion coefficients and thermodiffusion (or Soret diffusion) coefficients were computed using their Lenard–Jones potentials and the kinetic theory of gases [25]. All of these models are available as part of the standard CFD-ACE+ software, the details of which may be obtained from the *CFD-ACE+ Theory Manual* [26]. Figure 8 shows the comparison between numerical and experimental results. It is clear that the match is excellent. The oscillations in the profile are the result of the triangles next to the wall not all being equal in size. This causes the diffusion length-scale, δ, at adjacent cell faces to be slightly different, consequently producing small oscillations in the deposition rate. The

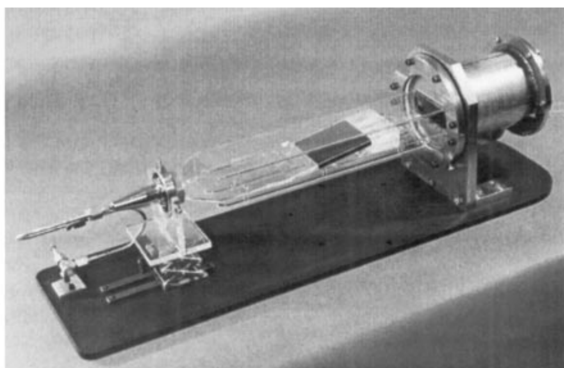

(a)

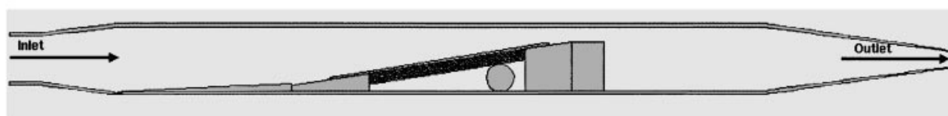

(b)

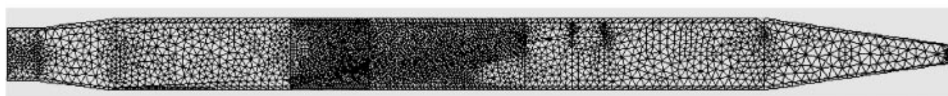

(c)

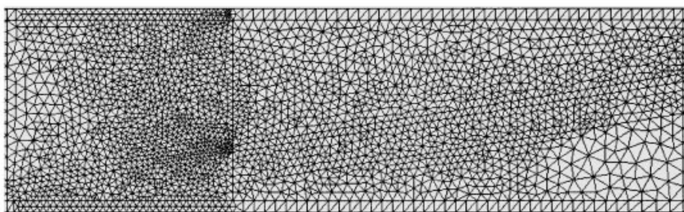

(d)

FIG. 7. Geometry (side view) and unstructured grid used for validation studies of the Crystal Specialties Model 425 horizontal MOCVD reactor. (a) Photograph of actual reactor. (b) Side view of reactor. The gray sections are made of fused silica, and the black section is the graphite substrate. (c) Unstructured triangular mesh of the whole geometry, which shows local refinement on the area around the substrate, especially just upstream of the substrate's leading edge. (d) Close-up of the grid around the substrate.

prediction of the "spike" in deposition at the leading edge of the substrate can be predicted only by tremendous grid refinement in that region. Such local refinement was easily possible with an unstructured triangular mesh (Fig. 7d), highlighting the advantage of using an unstructured mesh. With the aid of the rigorous mathematical treatment of surface reactions described in this article, it is now possible to model the entire computational domain using an unstructured mesh. This was not considered a feasible option until now because of the difficulty in implementing surface reaction boundary conditions for unstructured meshes.

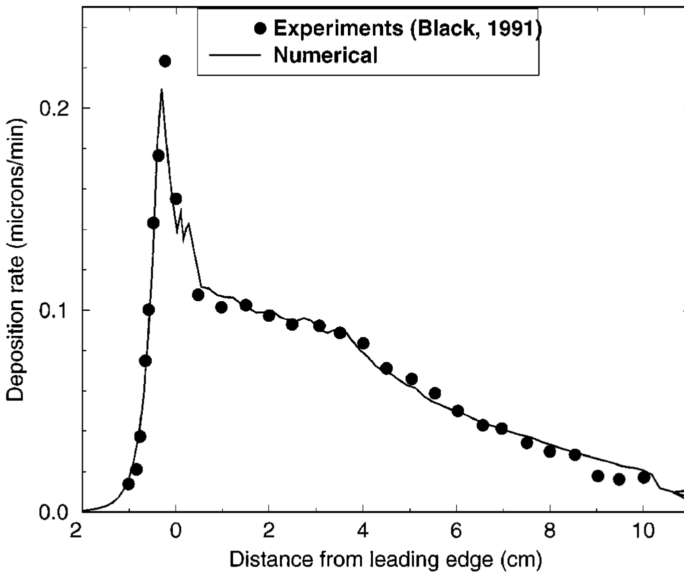

FIG. 8. Comparison of numerical predictions against experimental data of Black *et al.* [4].

4. CONCLUSIONS

A rigorous and robust numerical scheme to treat surface reaction boundary conditions has been presented and demonstrated in this article. The general practice in modeling CVD reactors, until now, was to model the interior of the reactor using a structured mesh. This poses problems for complex geometry and makes local grid refinement difficult. Using the numerical procedure described above, it is now possible to model the reactor interior using an unstructured mesh. This is useful particularly for modeling commercial MOCVD reactors, where it is necessary to model not only the reactor interior but also its exterior, which typically consists of complex 3D helical coils that are practically impossible to model using structured grids.

ACKNOWLEDGMENT

The support of the National Science Foundation through an SBIR Phase II grant (Contract DMI 9983415, Program Officer: Ms. Jean Bonney) is gratefully acknowledged.

REFERENCES

1. G. B. Stringfellow, *Organometallic Vapor-Phase Epitaxy: Theory and Practice* (Academic Press, San Diego, 1999).
2. D. H. Reep and S. K. Ghandhi, Deposition of GaAs epitaxial layers by organometallic CVD, *J. Electrochem. Soc.* **130**, 675 (1983).
3. K. F. Jensen, D. I. Fotiadis, and T. J. Mountziaris, Detailed models of the MOVPE process, *J. Cryst. Growth* **107**, 1 (1991).
4. L. R. Black, I. O. Clark, B. A. Fox, and W. A. Jesser, MOCVD of GaAs in a horizontal reactor; modeling and growth, *J. Cryst. Growth* **109**, 241 (1991).
5. F. Durst, L. Kadinskii, M. Peric, and M. Schafer, Numerical study of transport phenomena in MOCVD reactors using a finite volume multigrid solver, *J. Cryst. Growth*. **125**, 612 (1992).

6. M. Dauelsberg, L. Kadinski, Y. N. Makarov, T. Bergunde, G. Strauch, and M. Weyers, Modeling and experimental verification of transport and deposition behavior during MOVPE of $Ga_{1-x}In_xP$ in the planetary reactor, *J. Cryst. Growth* **208**, 85 (2000).
7. A. G. Salinger, J. N. Shadid, S. A. Hutchinson, G. L. Hennigan, K. D. Devine, and H. K. Moffat, Analysis of gallium arsenide deposition in horizontal chemical vapor deposition reactor using massively parallel computations, *J. Cryst. Growth* **203**, 516 (1999).
8. A. Krishnan and N. Zhou, Analysis of chemical vapor deposition in industrial reactors, presented at the Fourth ASME/JSME Thermal Engineering Conference, Honolulu Hawaii, March 19–24, 1995.
9. A. Ern, V. Giovangigli, and M. D. Smooke, Numerical study of a three-dimensional chemical vapor deposition reactor with detailed chemistry, *J. Comput. Phys*. **126**, 21 (1996).
10. N. K. Ingle, C. Theodoropoulos, T. J. Mountziaris, R. M. Wexler, and F. T. J. Smith, Reaction kinetics and transport phenomena underlying the low-pressure metalorganic chemical vapor deposition of GaAs, *J. Cryst. Growth* **167**, 543 (1996).
11. M. Coltrin, R. Kee, and F. Rupley, Surface chemkin: A general formalism and software for analyzing heterogeneous chemical kinetics at gas-solid interfaces, *Int. J. Chem. Kinet*. **23**, 1111 (1991).
12. A. N. Jansen, M. E. Orazem, B. A. Fox, and W. A. Jesser, Numerical study of the influence of reactor design on MOCVD with a comparison to experimental data, *J. Cryst. Growth* **112**, 316 (1991).
13. Y. Li and L. J. Giling, Influence of the temperature of the reactor top wall on growth processes in horizontal MOVPE reactors, *J. Cryst. Growth* **156**, 177 (1995).
14. M. Tirtowidjojo, and R. Pollard, Elementary processes and rate-limiting factors in MOVPE of GaAs, *J. Cryst. Growth* **93**, 108 (1988).
15. M. Tirtowidjojo, and R. Pollard, The influence of reactor pressure on rate-limiting factors and reaction pathways in MOVPE of GaAs, *J. Cryst. Growth* **98**, 420 (1989).
16. A. P. Peskin and G. R. Hardin, Gallium arsenide growth in a pancake MOCVD reactor, *J. Cryst. Growth* **186**, 494 (1998).
17. P. V. Hyer, Use of infrared imagery in characterization of chemical vapor deposition reactors, *Infrared Phys. Technol.* **38**, 17 (1997).
18. P. B. Chinoy and S. K. Ghandhi, Design considerations for the elimination of recirculation in horizontal epitaxial reactors, *J. Cryst. Growth* **108**, 105 (1991).
19. F. Nembri, A. Bossi, S. Ermakov, and P. G. Righetti, Isoelectrically trapped enzymatic bioreactors in a multimembrane cell coupled to an electric field: Theoretical modeling and experimental validation with urease, *Biotechnol. Bioeng*. **53**, 110 (1997).
20. J. Mantzaras, C. Appel, P. Benz, and U. Dogwiler, Numerical modelling of turbulent catalytically stabilized channel flow combustion, *Catal. Today* **59**, 3 (2000).
21. L. R. Laxminarayan, R. J. Kee, O. Deutschmann, J. Warnatz, and L. D. Schmidt, A critical evaluation of Navier-Stokes, boundary-layer, and plug-flow models of the flow and chemistry in a catalytic-combustion monolith, *Catal. Today* **59**, 47 (2000).
22. S. Mazumder and S. A. Lowry, Modeling commercial MOCVD reactors: Role of complex chemistry models, in *Proceedings of the SPIE, 2000*, (SPIE Publications, 2000) Vol. 3944–46, pp. 423–434.
23. S. Mazumder and A. Kersch, A fast Monte Carlo scheme for thermal Radiation in semiconductor processing applications, *Numerical Heat Transfer: Part B* **37**, 185 (2000).
24. S. Mazumder and A. Kersch, Effect of thin films on radiative transport in chemical vapor deposition systems, in *Proceedings of the ASME 1999*, (ASME Publications, 1999) HTD-Vol. 364–3, p. 9.
25. R. B. Bird, W. Stewart, and E. N. Lightfoot, *Transport Phenomena* (Wiley, New York, 1960).
26. *CFD-ACE+ Theory Manual* (CFD Research Corporation, Huntsville, 2001).